Jarosite formation in deep Antarctic ice provides a window into acidic, water-limited weathering on Mars

Giovanni Baccolo[1,2*], Barbara Delmonte[1], P. B. Niles[3], Giannantonio Cibin[4], Elena Di Stefano[1,2,5], Dariush Hampai[6], Lindsay Keller[3], Valter Maggi[1,2], Augusto Marcelli[6,7], Joseph Michalski[8], Christopher Snead[9] and Massimo Frezzotti[10]

[1]Department of Environmental and Earth Sciences, University of Milano-Bicocca, 20126, Milan, Italy
[2]INFN, section of Milano-Bicocca, 20126, Milan, Italy
[3]NASA Johnson Space Center, TX 77058, Houston, USA
[4]Diamond Light Source, Harwell Science and Innovation Campus, Didcot OX11 0DE, UK
[5]Department of Physical, Earth and Environmental Sciences, University of Siena, 53100, Siena, Italy
[6]Laboratori Nazionali di Frascati, Istituto Nazionale di Fisica Nucleare, 00044 Frascati, Italy
[7]Rome International Center for Materials Science - Superstripes, 00185 Rome, Italy
[8]Department of Earth Sciences, University of Hong Kong, Hong Kong
[9]Jacobs, NASA Johnson Space Center, TX 77058, Houston, USA
[10]Department of Science, University Roma Tre, Rome, Italy

* corresponding author: giovanni.baccolo@unimib.it

Abstract

Many interpretations have been proposed to explain the presence of jarosite within Martian surficial sediments, including the possibility that it precipitated within paleo-ice deposits owing to englacial weathering of dust. But until now a similar mechanism was not observed on Earth nor in other planetary settings. We report the first multi-analytical indication of jarosite formation within deep ice. Below 1000 m depth, jarosite crystals adhering on residual silica-rich particles have been identified in the Talos Dome ice core (East Antarctica) and interpreted as products of weathering involving aeolian mineral dust and acidic atmospheric aerosols. The progressive increase of ice metamorphism and re-crystallization with depth favours the relocation and concentration of dust and acidic brines in isolated environments, allowing chemical reactions and mineral neo-formation to occur. This is the first described englacial diagenetic mechanism occurring in deep Antarctic ice. It supports the ice-weathering model for jarosite formation on Mars,

highlighting the geologic importance of paleo ice-related processes on this planet. Additional implications concern the preservation of dust-related signals in deep ice cores with respect to paleoclimatic reconstructions and the englacial history of meteorites from Antarctic blue ice fields.

1. Introduction

Jarosite, a ferric-potassium hydroxide sulphate [$KFe^{3+}_3(SO_4)_2(OH)_6$], was firstly hypothesized to be a common mineral on Mars by Burns [1] despite its rareness on Earth. In 2004 the Opportunity rover reported widespread jarosite at Meridiani Planum [2], confirming Burns' prediction, but the geological context where jarosite was found -in fine-grained sediments within layered formations- was difficult to interpret. Since then, the mineral has been repeatedly identified on Mars [3, 4, 5] and has been regarded as an evidence for the occurrence of liquid water [6] because on Earth jarosite forms as the result of low temperature acidic-oxidative weathering of iron-bearing minerals in presence of limited water [7].

The long-term preservation of jarosite requires arid conditions because prolonged water activity results in its dissolution [8]. The occurrence of jarosite on Mars has thus been explained assuming that weathering fluids have been active for a geologically short time interval [9]. An apparent paradox concerns the lithology of the protolith in which jarosite occurs, which is composed of mafic (basaltic) volcanic material [10, 11]. The interaction between basalt and acidic solutions has a neutralizing effect incompatible with jarosite formation [12]. The paradox is solved if the interaction occurs in environments isolated from bedrock, where water-rock interaction is limited and low pH is maintained during the diagenesis [13].

Most of the hypotheses about the formation of Martian jarosite involve the interaction between acidic fluids and weathered sediments in transient lacustrine-evaporative basins similar to Earth playas [3, 5, 10] or volcanic settings, such as fumaroles [11]. An additional proposal predicted that jarosite formation would occur during weathering of mafic dust or fine-grained ash trapped in massive ice, but this had not been observed until now [13, 14]. The ice-weathering model suggested that the interior of ice deposits promotes acidic weathering of dust through cryo-concentration of sulfur-rich volcanic aerosols and result in the precipitation of jarosite [12, 13]. Experimental evidence has since shown that the weathering rate of basalt-related minerals is elevated at cryogenic temperature [15], in accordance with the identification of jarosite as weathering product in Antarctica [16]. But this hypothesis has remained a speculation until now. Until this work, Antarctic jarosite has been found in rock varnishes and weathering rinds formed on the surface of erratics [16] and of meteorites collected at blue ice fields [17, 18], or in soils developed from sulfide-rich rocks [19].

We report the identification of jarosite recovered from deep Antarctic ice, which we hypothesize as authigenic, resulting from the interaction between aeolian dust and acidic species trapped in the ice. Our results show that weathering and englacial diagenesis is possible deep inside thick ice, potentially affecting the climatic interpretation of dust records in deep ice cores. Given the similarities between our hypothesis and the Martian ice-weathering model, our findings support that ice-mediated weathering is a viable geological mechanism for jarosite formation on Mars, with major implications for past chemical weathering processes on the planet.

The Talos Dome ice core

The 1620 m long TALDICE (Talos Dome Ice Core 72°49′S, 159°11′E; 2315 m a.s.l.) has been retrieved from a peripheral ice dome of the East Antarctic Plateau [20] and dated up to 1439 m deep, where the estimated ice age is ~153,000 years before present (BP) [21, 22] (Figure 1). The deeper part of the core is believed to contain climatic information extending to 250,000 years BP and possibly beyond [20]. Below 1439 m depth, millimetric visible layers (volcanic ash and cloudy bands) are progressively tilted and folded, and deeper than 1528 m they disappear. In addition, below 1590 m very large ice-crystals (40-50 cm), indicative of ice metamorphism, have been observed [23] (Figure 1a). Such features depend on the bedrock characterizing the drilling site, whose morphology consists in mesas interrupted by canyons, disturbing the ice-flow [23]. Multiple lines of evidence suggest that throughout the late Quaternary the aeolian dust deposited at Talos Dome was mostly local, in particular during interglacials, when the arrival of dust from remote sources was suppressed [24]. The most important local sources of dust consist in high-elevation ice-free doleritic-basaltic outcrops [24, 25] and by tephra from proximal Antarctic volcanoes [26]. The influence of volcanic activity at Talos Dome is notable. More than 100 volcanic horizons have been identified along the core, with a frequency one order of magnitude greater than the one found in inner East Antarctica [27]. In addition, the aeolian reworking of volcanic deposits provides a background of volcanic tephra in the atmosphere which is also found in TALDICE [26].

2. Discussion

2.1. Identification of jarosite in Antarctic ice

The K-edge absorption energy of the Fe fraction of mineral dust from TALDICE increases with depth (Figure 1c), suggesting a progressive Fe oxidation [28]. Samples from the 0-1000 m (n=20), 1000-1300 m (n=18) and 1300-1620 m (n=16) depth intervals present average Fe K-edge absorption energies of 7125.5(0.5), 7126.5(0.4) and 7127.2(0.3) eV (standard deviation) respectively. Considering that the positive shift between $Fe^{2+}$and Fe^{3+} is 4 eV, the one observed along TALDICE corresponds to a 30-40 % increase of Fe^{3+} [28]. Data agree with the absolute determination of Fe

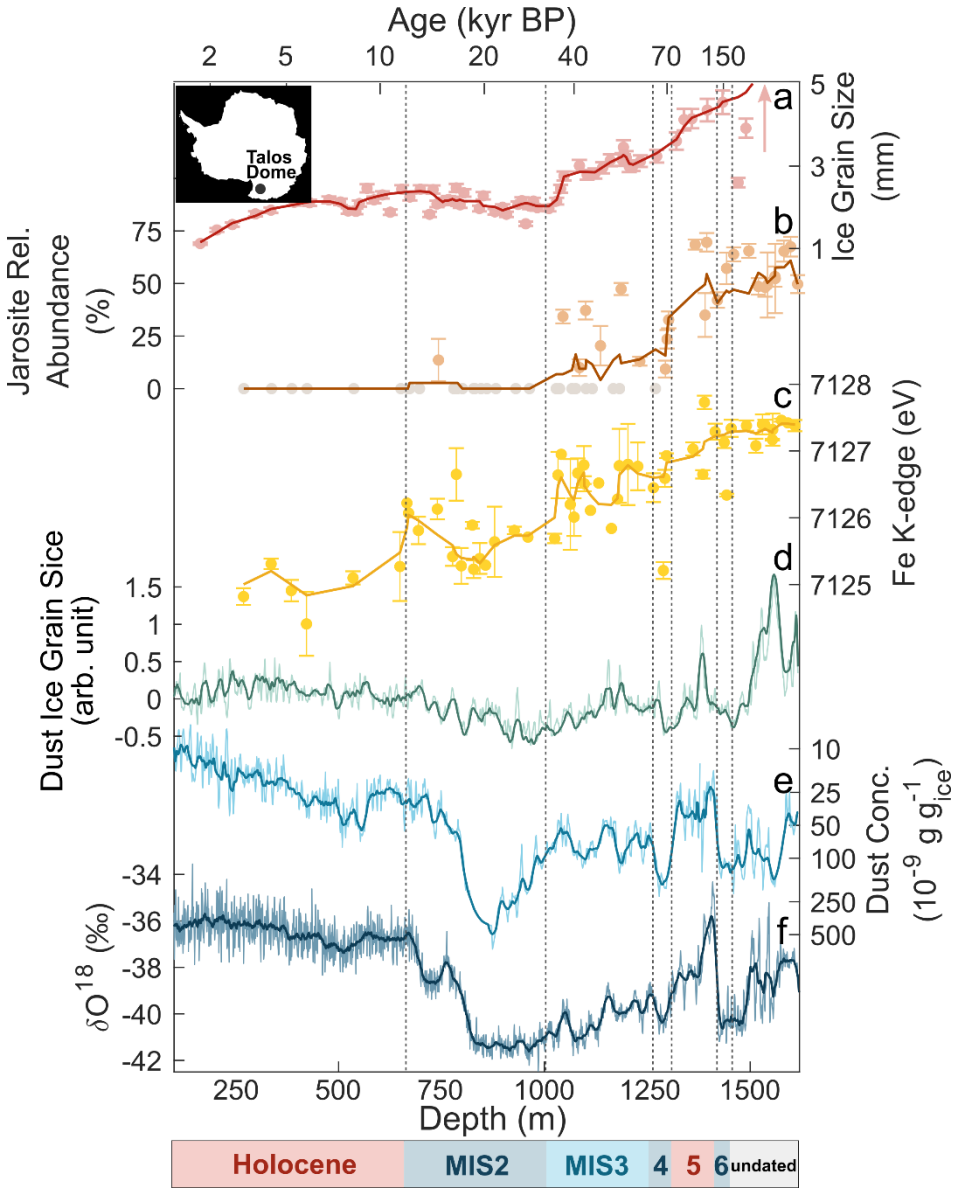

Figure 1 Records from the Talos Dome ice core. a) Ice-grain size; data from Montagnat et al. [23]. b) Jarosite relative abundance in dust extracted from TALDICE; grey dots refer to samples where jarosite is not recognized. c) Energy position of the K-edge X-ray absorption line of the iron fraction within TALDICE dust. d) Dust grain size index; developed to highlight the granulometric anomalies observed in dust from the deepest part of TALDICE. e) Concentration of insoluble mineral dust in ice samples along TALDICE: part of the data from Albani et al. [54]. f) TALDICE $\delta^{18}O$ record; data from Stenni et al. [20]. The AICC2012 chronology [21, 22] has been used to prepare the figure. The lower bar refers to the Marine Isotopic Stages (MIS) covered by TALDICE.

oxidation in TALDICE dust: between 0 and 1000 m Fe in mineral dust consists in a 70-30 % mix of Fe^{3+}- Fe^{2+}, while below 1500 m only Fe^{3+} is detected [29]. The trend is indicative of oxidative weathering and involves the core throughout its length with the exception of the deepest part, where the absorption energy presents a plateau at about 7127 eV, consistent with a complete oxidation of Fe. Another evidence of weathering comes from the identification of jarosite within TALDICE dust (Figure 1b). Above the depth of 1033 m, only 1 of 22 samples presents evidence of jarosite occurrence. Fe K-edge absorption spectra of shallow samples are in fact reproduced using common iron bearing minerals, such as oxides, phyllosilicates, silicates (Figure S1). At greater depth a convex feature at 7138 eV, indicative of jarosite [29], appears in X-ray absorption (XAS) spectra (Figure S1) and accordingly between 1033 and 1500 m the contribution of this mineral increases and becomes dominant, meaning that more than 50 % of the information from XAS spectra is reproduced by jarosite. Below 1500 m jarosite contribution maintains a stable value with a mean of 54(8) % (standard deviation), similarly to what observed for Fe oxidation. The agreement between the records is expected given that jarosite is a ferric mineral.

The morphology and elemental composition of mineral dust from sections of TALDICE deeper than 1500 m has been investigated through scanning Electron Microscopy (SEM) coupled with energy dispersive X-ray spectroscopy (EDX) (Figure 2). Weathering features are observed, including the presence of micrometric to sub-micrometric-sized

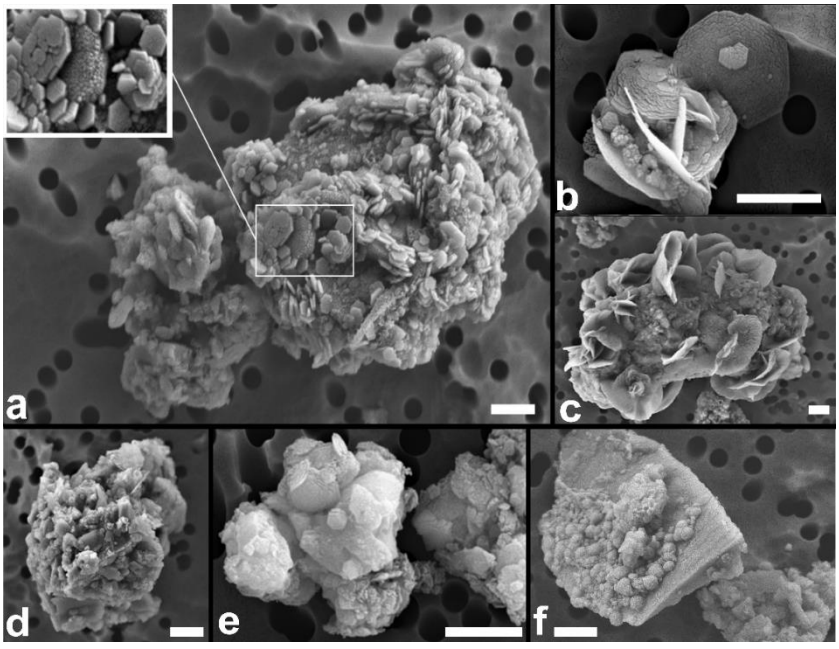

Figure 1 SEM images of dust grains extracted from TALDICE sections at 1,560 m depth (a, c, d, f) and 1534 m depth (b, e). Scale bar: 1 µm.

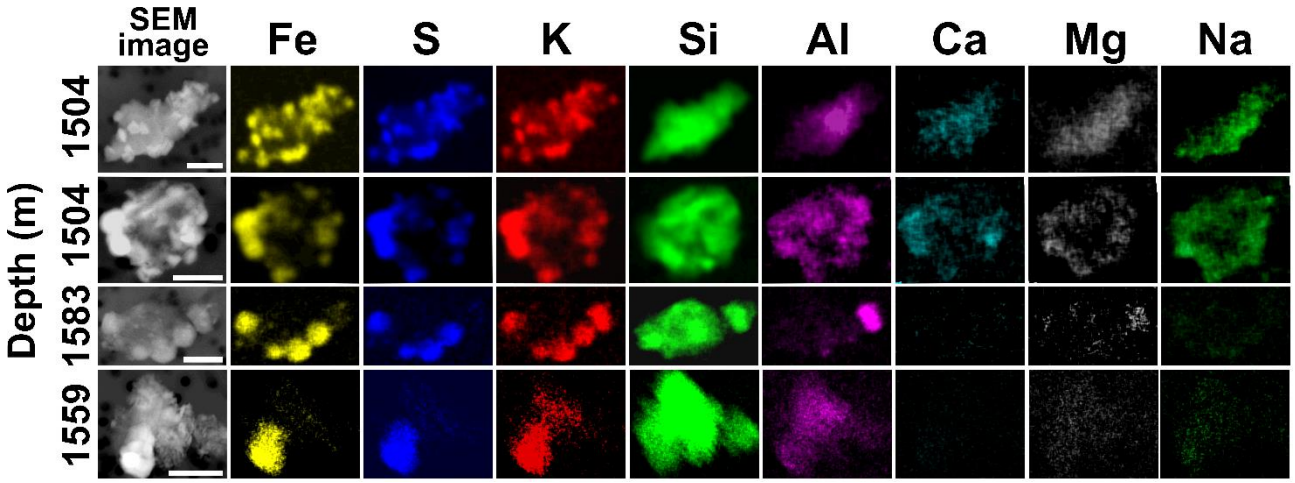

Figure 3 Elemental maps obtained through SEM-EDX of dust grains from deep TALDICE ice. Scale bar: 2 µm.

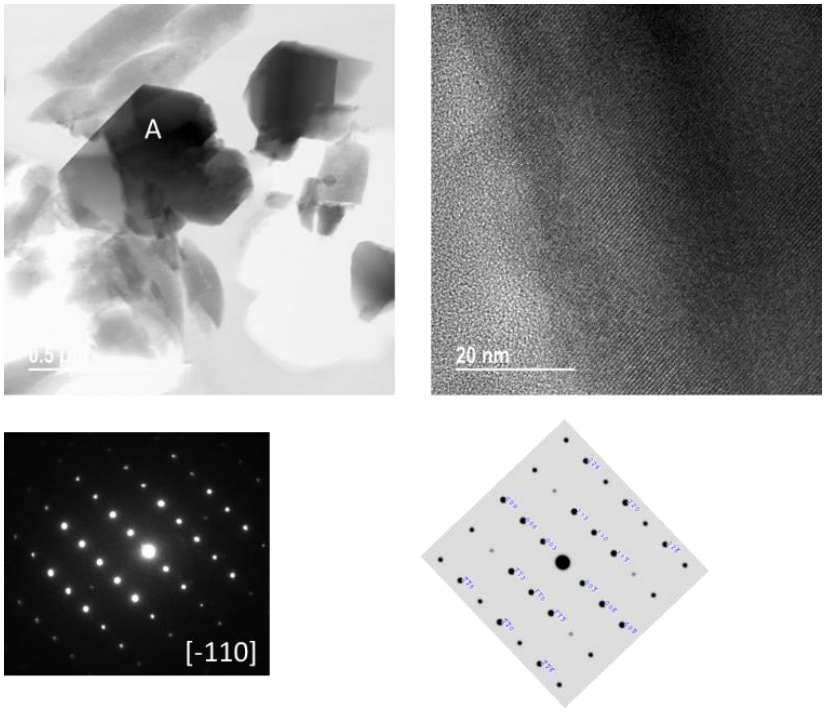

115

Figure 4. Brightfield STEM image and a selected area of electron diffraction (SAED) pattern from the crystal labelled A. The SAED pattern is from the [-110] zone axis of jarosite.

precipitates ranging from crystalline minerals (Figure 2a, b, c) to globular concretions presenting irregular surface cracks and poorly ordered aggregates (Figure 2d, e, f) and scarcity of grains with sharp edges. Only a few volcanic glasses, covered by precipitates are recognized (Figure 2f). Among the precipitates, hexagonal platelets are frequently observed, either as independent crystals (Figure 2a) or grouped and often organized in rosettes (Figure 2b, c), a habit compatible with the trigonal system of jarosite [30]. The morphology of TALDICE deep particles exhibits differences with the ones from the upper core, consisting in micrometric mono-mineral particles and volcanic glasses exhibiting a fresh texture (Figure S2). Elemental maps of individual grains show that precipitates are composed by Fe, S and K, corresponding to jarosite constituents, while grain cores mostly consist in Si or Si and Al, with minor traces of Ca, Mg and Na (Figure 3). A definitive confirmation that precipitates in deep TALDICE consist of jarosite comes from Transmission Electron Microscopy (TEM-EDX) analyses carried out on two mineral grains from TALDICE samples 1559 m deep. Results confirm the presence of jarosite as sprays/rosettes of bladed crystals with diffraction spacings and chemical composition consistent with jarosite (Figure 4). The examined crystals are nearly pure $KFe^{3+}_3(SO_4)_2(OH)_6$ as supported by EDX quantitative results (Table S1).

2.2. Englacial chemical weathering of mineral dust in deep ice

Physico-chemical signals are preserved for hundreds of thousands of years within ice [31]. Climatic proxies, such as $\delta^{18}O$ and dust concentration, are correlated in ice cores and show coherent oscillations during glacial/interglacial cycles [32]. This is confirmed by TALDICE data, where their linear R-squared, when considering the depth interval 0-1400 m, is 0.75 (Figure S5). In contrast, Fe oxidation and jarosite abundance are not coupled with $\delta^{18}O$ ($R^2 < 0.02$, Figure S5) and lack of climate-related fluctuations. They are correlated with the increasing size of ice crystals along the core (R^2 = 0.55 and 0.49 respectively, Figure S5), which depends on ice metamorphism and not on climate [33]. Being jarosite observed in the deep part of TALDICE, it could be argued that the mineral comes from the bedrock. Where TALDICE was retrieved, ice thickness is 1795 m but drilling stopped at 1620 m [20]. It is unlikely that jarosite, which is found from 1000 m to the end of the core, is sourced by the bedrock. Only an extreme folding could explain the presence of bedrock inclusions hundreds of m above the interface, but this is incompatible with the preservation of ice stratigraphy up to 1560 m deep [20].

Based on our understanding of the environmental conditions present inside the ice, we interpret jarosite as product of englacial weathering. Its formation requires acidic conditions, a limited activity of liquid water and the presence of Fe-bearing materials [7]. The deep part (> 1000 m) of TALDICE can meet such requirements. Deep ice is affected by a progressive re-crystallization of the ice grains [33, 34]. A consequence of re-crystallization is that impurities incompatible within the ice lattice accumulate at ice grain junctions [35] or within intra-grain µ-inclusions [34, 36]. Atmospheric

sulphates and sulfuric acid are strongly affected by remobilization in ice [35, 37]. They are easily concentrated in isolated environments forming acidic brines whose eutectic temperature is below the pressure melting point of deep ice, allowing for the presence of aqueous fluids in the form of localized brines [35, 34, 37, 38]. In deep ice, as a result of the increased temperature and ice metamorphism, the concentration and mobilization of impurities allows for the mixing of soluble and insoluble species, and for their interaction through englacial acid-base reactions [34, 36, 39, 40]. Such small-scale environments promote chemical weathering of aeolian dust [36]. In addition, dust particles deposited at Talos Dome have a basaltic/doleritic signature and are rich in Fe [25, 26], making deep TALDICE an environment suitable for jarosite precipitation. The identification of secondary ferric precipitates in deep ice is not completely new, evidences were reported from the two EPICA ice cores: De Angelis et al. [34] observed micrometric Fe-oxides precipitates within the Dome C ice core while Eichler et al. [36] interpreted a few micro-inclusions as jarosite in the Dronning Maud Land ice core.

The acidic weathering of basalt in a closed system produces jarosite and amorphous silica [6, 12]. This matches the observed composition of the grains observed in deep TALDICE. Jarosite is attached to grains composed almost entirely of Si with detectable Al (Figure 3), a signature compatible with amorphous silica with substituted Al. The distribution of other elements further supports chemical weathering in deep TALDICE: Mg, Ca and Na are almost absent from jarosite precipitates and scarce within Si-rich grains (Figure 3). The scarcity of these elements, common constituents of minerals, suggests that reaction with acidic species lead to formation of soluble compounds which were removed during the preparation of samples through filtration. This is supported by the identification in deep ice cores of soluble Mg, Ca and Na sulphates [36, 39, 40] and by their direct observation in TALDICE when ice is sublimated rather than being filtrated [41]. Weathering of minerals also impacts the grain size of insoluble dust in deep TALDICE. This is shown by the dust grain size index, developed to distinguish upper and deeper TALDICE dust through granulometric features (Figure 1d). Dust from deep TALDICE presents an excess of large particles and a lack of fine ones with respect to typical dust from Antarctic ice cores (Figure S6), as highlighted by the index which presents positive values only in the bottom part of TALDICE (see the Supplementary for details). Such anomalies can relate to the chemical aggregation of mineral particles resulting from jarosite englacial precipitation. This mineral is in fact known for acting as a cement during weathering, favoring the aggregation of particles [30]. We observe that below 1400 m, the linear R-squared between $\delta^{18}O$ and dust decreases from 0.75 to 0.44 (Figure S5), pointing to a partial degradation of the climatic significance of the TALDICE dust record.

2.3. Antarctic implications

Jarosite formation in TALDICE constrains the physico-chemical environment of deep Antarctic ice. Antarctic ice, thanks to volcanogenic and biogenic sulfuric acid, presents a pH between 5.5 and 6 [42], but jarosite formation requires a pH lower than 4 [6] which can only be reached through concentration of acids mediated by ice re-crystallization. Another important point concerns the occurrence of liquid water in the form of brines. Only a few direct lines of evidence for its presence in ice cores are available [37], although questioned [36], but theoretical supports exist [38]. The discrepancy could arise because acidic brines are likely stable at the pressure and temperature conditions found in deep ice sheets, not at the laboratory ones. Yet, the occurrence of jarosite, whose formation requires liquid water, is a strong evidence for the actual occurrence of aqueous brines in deep ice, likely in correspondence of ice grain junctions or at intra-grain micro-inclusions. In TALDICE jarosite is present below the depth of 1000 m, suggesting that its formation is associated with a threshold (Figure 1b). Since jarosite forms also at the Earth surface, high pressure is likely not the limiting factor [7]. Ice temperature at 1000 m depth at Talos Dome is ca. -25°C, while at the core bottom it is -10°C (Rix & Martin, personal communication). Increasing temperature could accelerate jarosite formation, but on Earth and Mars it is stable at either colder and warmer temperatures with respect to these values [7]. The actual limiting factor is probably ice metamorphism -only indirectly related to pressure and temperature [33, 23]- which favors concentration of impurities, formation of brines, and weathering of minerals. Reactions involving dust in deep ice should be investigated further in relation to the preservation of climatic signals in deep ice cores, in particular considering the “quest for the oldest ice”. Ice core records which could be significantly affected by the processes described here, are the ones related to Fe oxidation and speciation [43].

Other implications of this study concern meteorites found at Antarctic blue ice fields. On the surface of such meteorites a weathering rind 10-100 μm thick rich in jarosite and amorphous silica is commonly found, pointing to acidic alteration [17]. The rinds have been explained assuming that weathering occurred once meteorites were exposed at the ice surface, because of the interaction with acidic atmospheric species and tiny amounts of liquid water during summer [17]. Meteorites from blue ice can have remained into the ice for tens of thousands of years, reaching deep portions of the Antarctic ice sheet before surfacing [44, 45, 18]. The interface between deep ice and meteorites could promote the occurrence of acidic aqueous brines because of the crystallographic misfits between ice and mineral structures. Given the compositional similarity between the rinds and weathered dust in deep TALDICE, we suggest that englacial weathering of meteorites is an important process. A support to this hypothesis comes from the Dome Fuji ice core, where jarosite has been found in correspondence of two extraterrestrial dust horizons [46]. In TALDICE, jarosite only forms below 1000 m deep; its presence in Antarctic meteorite rinds could be thus be interpreted as a proxy of the

englacial depth reached by meteorites themselves and of their residence time into the ice, as originally proposed by Terada et al. [18].

2.4. Martian implications

The occurrence of jarosite in TALDICE supports the ice-weathering model for the formation of Martian jarosite within large ice-dust deposits [13]. The environment inside the Talos Dome ice is isolated from the Earth atmosphere and its conditions, including pressure, temperature, pH, and chemistry, provides a suitable analogue for similar Martian settings. Dust deposited at Talos Dome is also similar to Martian atmospheric dust, being both mostly basaltic [10, 11]. Within thick ice deposits it is likely that the environment would be similar at Talos Dome and under Mars-like conditions since both settings would contain at cryogenic temperatures basaltic dust and volcanogenic and biogenic (for Antarctic only) sulfur-rich aerosols. What set them apart is the oxidative agent responsible for Fe oxidation. In deep TALDICE, Fe is likely oxidized through the interaction between air bubbles and clathrates and mineral dust. On Mars oxygen is likely derived from aerosols such as oxy-chlorine species formed through UV photo-oxidation [47]. Considering this context, it is reasonable that the formation of jarosite on Mars involves the interaction between brines and mineral dust in deep ice, as observed in TALDICE. This mechanism for Martian jarosite precipitation is paradigm changing and strongly challenges assumptions that the mineral formed in playa settings [3, 5, 10].

Mars experienced dramatic climate swings and glaciations throughout its history [48, 49], and it has been argued that much of the physical layering observed on Mars surface could have been mediated by paleo ice-related processes [50]. In fact, the Martian polar regions exhibit materials rich in sulphates created during the seasonal accumulation and aeolian reworking of sublimation residues [51, 52]. Despite Burns' prophetic vision of Mars low-temperature, acid, water-limited alteration [1], ice mediated weathering has never been widely embraced or tested. Based on ongoing detections across the planet, jarosite is probably globally distributed across Mars in association with finely layered sediments [3, 4, 5]. Such sediments could result from the accumulation of weathered sublimation residue of past ice-rich deposits, since most of the settings where they occur are compatible with alteration pathways enabled by deep ice metamorphism and cryo-concentration of acidic fluids [13, 14]. In contrast, recent studies have shown that the playa model does not adequately explain the chemical characteristics of jarosite rich deposits, their enormous size, and the location of the putative playas [11, 13, 53].

3. Acknowledgment

This work is part of the TALDEEP project funded by MIUR (PNRA18_00098). The Talos Dome Ice core Project (TALDICE), a joint European programme, is funded by national contributions from Italy, France, Germany, Switzerland and the United Kingdom. Primary logistical support was provided by PNRA at Talos Dome. This is TALDICE publication no **xx**. This publication was generated in the frame of Beyond EPICA – Oldest Ice (BE-OI). The project has received funding from the European Union's Horizon 2020 research and innovation programme (grant no. 815384). The authors acknowledge Diamond Light Source for provision of beamtime within proposals sp7314, sp8372 and sp9050. We thank Paolo Gentile and Tiziano Catelani for their assistance with SEM and for providing mineral specimens. Support from NASA ISFM grants to Johnson Space Center are also acknowledged.

4. Conflict of interest

The authors declare no conflict of interest.

5. Author contributions

GB and BD conceived the idea of the work; GB interpreted the data and wrote the paper with contributions from all the coauthors; GB, BD, EDS prepared the samples and carried out Coulter counter measurements and SEM; GB, GC, Dh, AM acquired and analyzed XAS data; LK, CS performed TEM analyses; PBN, JM, MF, VM helped in the interpretation and discussion of data.

6. Methods

Dust concentration and grain size in TALDICE have been determined through Coulter counter technique in the ISO6 clean room available at the EUROCOLD facility of the University Milano-Bicocca. Twenty-five cm-long ice sections were decontaminated with three successive baths in MilliQ water (© Millipore) and mixed with a clean electrolyte solution (NaCl solution, passed through 0.22 µm pore size membranes) until a final Na^+ concentration of 1 % m/m was reached. The passage is required so as to make samples electrically conductive. Each sample, consisting in 10 mL of decontaminated meltwater, was measured two or three times (depending on sample availability) with a Beckman Multisizer 4 equipped with a quartz tube equipped with a 30 µm orifice. Such an instrumental apparatus allows for the quantification of the insoluble particles with a spherical equivalent diameter between 0.6 and 18 µm, divided into 400

channels. Volume of insoluble particles was then converted into mass using a constant density of 2.5 g cm^{-3}, following the convention suggested by Hänel [55] for mineral aerosols and classically adopted by the ice core community [56, 57]. Blanks were constantly evaluated during the analysis, their signal, on average, corresponded to 2.5 % of the mean sample one. Standard deviation of the replicates ranged between 5 and 10 % with respect to the total dust mass of samples. Data concerning the highest part of TALDICE (0-900 m depth interval) have already been published [25, 54], data from the lowest part (from 900 m to 1616 m) are published here for the first time.

Dust grain size index. To highlight the granulometric differences between dust samples from the upper and lower sections of TALDICE, a dedicated index was developed. For each dust sample analyzed with Coulter counter, sixteen granulometric variables were defined, consisting in dust concentration and ratios referred to specific grain size intervals (Supplementary). Surficial samples are typically fitted by a log-normal distribution, with modal values ranging between 1.8 and 2.2 µm, and present a limited tail of coarser particles (5-10 µm) related to the influence of local Antarctic dust sources [25, 54]. Deeper samples show a coarser modal value (between 2 and 4 µm) but are poorly described by log-normal distributions because of the presence of evident tails of coarse particles and the scarcity of finer ones (< 2 µm). Examples are reported in Figure S6. A Partial Least Square – Discriminant Analysis algorithm was applied [58] to highlight such differences. Samples were firstly classified into upper (0-1450 m depth interval) and lower (1450-1620 depth interval), the algorithm was therefore instructed to reproduce the classification using the descriptive granulometric variables calculated from Coulter counter data, without considering the depth of samples. The dust grain size index shown in Figure1d corresponds to the linear combination of the granulometric variables defined by the first latent component calculated by the model to classify the samples. Further details are found in the Supplementary.

Fe K-edge absorption energy was determined through XAS, performed at B18 beamline of the Diamond Light Source [59]. Analyses were carried out on samples prepared extracting mineral particles from decontaminated meltwater obtained from TALDICE ice sections in an ISO6 clean room. The extraction took place with clean polycarbonate membranes (rinsed with high purity nitric acid, pore-size 0.4 µm) where meltwater was passed through with micro-pipettes, so as to concentrate the particles in the smallest possible area and maximize the performances [60]. For each sample a variable volume of meltwater was filtered depending on dust concentration (evaluated with Coulter counter), so as to have on each filter not less than 2-3 µg of dust. Membranes where dust was deposited were placed in clean PTFE filter-holder and mounted on the beamline. Fifty-four samples were prepared, covering the entire length of the ice core; details, including spectral data, are reported in the Supplementary. To avoid contamination and interference issues the following procedures were adopted: 1- the experimental chamber was provided with a clean glove-box filled with pure nitrogen in order to handle and mount the samples in clean conditions; 2- the inner walls of the chamber were

coated with clean plastic sheets to reduce the inelastic scattering produced by the interaction of the beam with the metallic chamber; 3- measurements were carried out under high vacuum conditions to remove atmospheric interferences. XAS spectra were acquired at the Fe K-edge absorption line in fluorescence mode, considering the energy interval between 7000 and 7500 eV and energy steps of 0.3 eV. A Vortex 4-elements silicon detector was used (spectral resolution 140 eV full width height maximum at the 5.9 keV Mn K-line). The energetic calibration was monitored through the repeated acquisition of the absorption edge spectrum of a metallic Fe foil. For each sample at least three spectra were acquired during different sessions and average spectra were calculated. Blank filters were measured but no Fe signal was detected. Standards (SRM 2709a, NIST) were prepared following the same procedures adopted for the samples to evaluate the precision of the method, which is 0.2 eV. Spectra were analyzed with the software Athena [61]. To make them comparable, fluorescence signals were processed to obtain absorption coefficients, which were normalized considering the post-edge baseline [62]. The pre-edge region was normalized subtracting the pre-edge baseline. The energy position of the Fe K-edge absorption was defined as the energy of the main absorption edge at the height of 0.8 (normalized value) with respect to the post-edge baseline Errors shown in Figure 1c correspond to the standard deviation calculated considering the replicates, further details are found in Cibin et al. [63].

Jarosite Abundance was estimated comparing the Fe-K edge spectral signature of the samples with the one of mineralogical standards [64]. Specimens of the following minerals were retrieved from the collection of the University Milano-Bicocca: biotite, chlorite, glaucophane, goethite, hematite, hornblende, jarosite, limonite, magnetite, muscovite, fayalite, pargasite, pyrite, schoerlite, siderite. Fragments of the minerals were powdered using a mortar and mixed with cellulose in pellets which were measured at B18 in transmission mode. Fe K-edge absorption spectra were processed following the steps adopted for samples. To determine the influence of jarosite within TALDICE samples, a linear combination fitting approach was followed [64]: spectra of the mineral standards were used to reproduce the spectra of the samples through the calculation of linear combinations with the combinatoric package of the Athena software [61], based on ordinary least square regression (OLS). For each sample spectrum, all the possible combinations of 4 standards were calculated, forcing the presence of goethite, being the most common Fe-bearing mineral within aerosols [65], in particular in cold environments [66, 67]. Jarosite relative abundance (Figure 1b) corresponds to the coefficients (expressed as %) associated to jarosite within each linear combination. The % coefficient varies between 0 and 100 and is interpreted as the relative amount of information present in sample spectra that is explained by jarosite signature. The associated error is only statistical and corresponds to the OLS standard error of jarosite regression coefficient. Further details are found in the Supplementary.

SEM-EDX observations were carried out on samples of dust extracted from TALDICE decontaminated meltwater, using a Zeiss Gemini 500 Field-Emission SEM equipped with EDX (Quantax EDX 4000, Bruker). Insoluble mineral dust was extracted from meltwater by filtration in an ISO6 clean room with polycarbonate membranes (diameter 25 mm, pore size 0.44 µm). After filtration some membranes were coated with gold for morphological observations (SEM) and others with graphite, for elemental mapping of mineral particles (SEM-EDX).

TEM-EDX observations Two samples were prepared for TEM and EDX analyses following the same procedure adopted for SEM-EDX. Dust particles from two deep sections of TALDICE (below 1500 m) were deposited on polycarbonate membranes through filtration and successively picked, embedded in low viscosity epoxy, and thin sections were placed on amorphous carbon support films and were analyzed using a JEOL 2500SE 200 kV field-emission scanning and transmission electron microscope (STEM) equipped with a JEOL silicon drift detector for EDX. Diffraction data from multiple orientations were obtained from selected areas of the grains to confirm their identity. Quantitative EDX data were obtained from the same grains as the diffraction data and were quantified using standard thin-film analysis techniques with k-factors from mineral standards (Table S1).

7. References

[1] Burns, R. G. Ferric sulfates on Mars. J. Geophys. Res. 92, E570-E574 (1987).

[2] Klingelhöfer, G. et al. Jarosite and Hematite at Meridiani Planum from Opportunity's Mössbauer Spectrometer. Science 306, 1740-1745 (2004).

[3] Farrand, W. H., Glotch, T. D., Rice Jr., J. W., Hurowitz, J. A., Swayze, G. A. Discovery of jarosite within the Mawrth Vallis region of Mars: Implications for the geologic history of the region. Icarus 204, 478-488 (2009).

[4] Weitz, C. M., Noe Dobrera, E., Wray, J. J. Mixtures of clays and sulfates within deposits in western Melas Chasma, Mars. Icarus 251, 291-314 (2015).

[5] Rampe, E. B. et al. Mineralogy of an ancient lacustrine mudstone succession from the Murray formation, Gale crater, Mars. Earth Planet. Sci. Lett. 471, 172-185 (2017).

[6] Elwood Madden, M. E., Bodnar, R. J., Rimstidt, J. D. Jarosite as an indicator of water-limited chemical weathering on Mars. Nature 431, 821-823 (2004).

[7] Papike, J. J., Karner, J. M., Shearer, C. K. Geochim. Cosmochim. Ac. 70, 1309-1321 (2006).

[8] Tosca, N. J., McLennan, S. M., Dyar, M. D., Sklute, E. C., Michel, F. M. Fe oxidation processes at Meridiani Planum and implications for secondary Fe mineralogy on Mars. J. Geophys. Res. Planets 113, E05005 (2008).

[9] Elwood Madden, M. E., Madden, A. S., Rimstidt, J. D. How long was Meridiani Planum wet? Applying a jarosite stopwatch to determine the duration of aqueous diagenesis. Geology 37, 635-638 (2009).

[10] McLennan, S. M. et al. Provenance and diagenesis of the evaporite-bearing Burns formation, Meridiani Planum, Mars. Earth Planet. Sci. Lett. 240, 95-121 (2005).

[11] McCollom, T. M. & Hynek, B. M. A volcanic environment for bedrock diagenesis at Meridiani Planum on Mars. Nature 438, 1129-1131 (2005).

[12] Zolotov, M. Y. & Mironenko, M. V. Timing of acid weathering on Mars: A kinetic-thermodynamic assessment. J. Geophy. Res. Planets 112, E07006 (2007).

[13] Niles, P. B. & Michalski, J. M. Meridiani Planum sediments on Mars formed through weathering in massive ice deposits. Nat. Geosci. 2, 215-220 (2009).

[14] Michalski, J. M. & Niles, P. B. Atmospheric origin of Martian interior layered deposits: Links to climate change and the global sulfur cycle. Geology 40, 419-422 (2012).

[15] Niles, P. B., Michalski, J., Ming, D. W., Golden, D. C. Elevated olivine weathering rates and sulfate formation at cryogenic temperatures on Mars. Nat. Comm. 8, 998 (2017).

[16] Giorgetti, G. & Baroni, C. High-resolution analysis of silica and sulphate-rich rock varnishes from Victoria Land (Antarctica). Eur. J. Mineral. 19, 381-389 (2007).

[17] Hallis, L. J. Alteration assemblages in the Miller Range and Elephant Moraine regions of Antarctica: Comparisons between terrestrial igneous rocks and Martian meteorites. Meteorit. Planet. Sci. 48, 165-179 (2013).

[18] Terada, K. et al. General Characterization of Antarctic Micrometeorites Collected by the 39th Japan Antarctic Research Expedition. Antarct. Meteorite Res. 14, 89-107 (2001).

[19] Simas, F. N. B. et al. Clay-sized Minerals in Permafrost-affected Soils (Cryosols) from King George Island, Antarctica. Clay. Clay Miner. 54, 721-736 (2006).

[20] Stenni, B. et al. Expression of the bipolar see-saw in Antarctic climate record during the last deglaciation. Nat. Geosci. 4, 46-49 (2011).

[21] Veres, D. et al. The Antarctic ice core chornology (AICC2012): an optimized multi-parameter and multi-site dating approach for the last 120 thousands years. Clim. Past 9, 1733-1748 (2013).

[22] Bazin, L. et al. An optimized multi-proxy, multi-site Antarctic ice and gas orbital chronology (AICC2012): 120-800 ka. Clim. Past 9, 1715-1721 (2013).

[23] Montagnat, M. et al. Measurements and numerical simulation of fabric evolution along the Talos Dome ice core, Antarctica. Earth Planet. Sci. Lett. 357-358, 168-178 (2012).

[24] Delmonte, B. et al. Aeolian dust in the Talos Dome ice core (East Antarctica, Pacific/Ross Sea sector): Victoria Land versus remote sources over the last two climatic cycle. J. Quaternary Sci. 25, 1327-1337 (2010).

[25] Baccolo, G. et al. Regionalization of the atmospheric dust cycle on the periphery of the East Antarctic ice sheet since the last glacial maximum. Geochem. Geophy. Geosy. 19, 3540-3554 (2018).

[26] Delmonte, B. et al. Modern and Holocene aeolian dust variability from Talos Dome (Northern Victoria Land) to the interior of the Antarctic ice sheet. Quaternary Sci. Rev. 64, 76-89 (2013).

[27] Narcisi, B., Petit, J.R., Delmonte, B., Scarchilli, C., Stenni, B. A 16,000 yr tephra framework for the Antarctic ice sheet: a contribution from the new Talos Dome core. Quat. Sci. Rev. 49, 52-63 (2012).

[28] Berry, A. J. et al. "XANES calibrations for the oxidation state of iron in a silicate glass" Am. Mineral. 88, 967-977 (2003).

[29] Baccolo, et al. G. The Contribution of Synchrotron Light for the Characterization of Atmospheric Mineral Dust in Deep Ice Cores: Preliminary Results from the Talos Dome Ice Core (East Antarctica). Condensed Matt. 3, 25 (2018).

[30] Long, et al. Formation of alunite, jarosite and hydrous iron oxides in a hypersaline system: Lake Tyrell, Victoria, Australia. Chem. Geol. 96, 183-202 (1992).

[31] EPICA Community Members. Eight glacial cycles from an Antarctic ice core. Nature 429, 623-628 (2004).

[32] Markle, B. R., Steig, E. J., Roe, G. H., Winckler, G., McConnell, J. R. Concomitant variability in high-latitude aerosols, water isotopes and the hydrologic cycle. Nat. Geosci. 11, 853-859 (2018).

[33] De La Chapelle, S., Castelnau, O., Lipenkov, V., Duval, P. Dynamic recrystallization and texture development in ice as revealed by the study of deep ice cores in Antarctica and Greenland. J. Geophys. Res. 103, 5091-5105 (1998).

[34] De Angelis, M., Tison, J. L., Morel-Fourcade, M. C., Susini, J. Micro-investigation of EPICA Dome C bottom ice: evidence of long term in situ processes involving acid–salt interactions, mineral dust, and organic matter. Quat. Sci. Rev. 78, 248-265 (2013).

[35] Mulvaney, R., Wolff, E. W., Oates, K. Sulphuric acid at grain boundaries in Antarctic ice. Nature 331, 247-249 (1988).

[36] Eichler, J. et al. Impurity analysis and microstructure along the climatic transition from MIS 6 into 5e in the EDML ice core using cryo-Raman microscopy. Front. Earth Sci. 7, 20 (2019).

[37] Fukazawa, H., Sugiyama, K., Mae, S., Narita, H., Hondoh, T. Acid ions at triple junction of Antarctic ice observed by Raman scattering. Geophy. Res. Lett. 25, 2845-2848 (1998).

[38] Dash, J. G., Rempel, A. W., Wettlaufer, J. S. The physics of premelted ice and its geophysical consequences. Rev. Mod. Phys. 78, 695-741 (2006).

[39] Ohno, H. et al. Physicochemical properties of bottom ice from Dome Fuji, inland East Antarctica. J. Geophys. Res. Earth Surf. 121, 1230-1250 (2016).

[40] Traversi, R. et al. Sulfate spikes in the deep layers of EPICA-Dome C ice core: Evidence of glaciological artifacts. Environ. Sci. Technol. 43, 8737-8743 (2009).

[41] Iizuka, Y. et al. Sulphate and chloride aerosols during Holocene and last glacial periods preserved in the Talos Dome Ice Core, a peripheral region of Antarctica. Tellus B 65, 20197 (2013).

[42] Legrand, M. J., Aristarain, A. J., Delmas, J. R. Acid titration of polar snow. Anal. Chem. 54, 1336-1339 (1982).

[43] Burgay, F. et al. Fe2+ in ice cores as a new potential proxy to detect past volcanic eruptions. Sci. Total Environ. 654, 1110-1117 (2019).

[44] Folco, L., Welten, K. C., Jull, A. J. T., Nishiizumi, K., Zeoli, A. Meteorites constrain the age of Antarctic ice at the Frontier Mountain blue ice field (northern Victoria Land). Earth Planet. Sci. Lett. 248, 209-216 (2006).

[45] Zekollari, H. et al. Unravelling the high-altitude Nansen blue ice field meteorite trap (East Antarctica) and implications for regional palaeo-conditions. Geochim. Cosmochim. Ac. 248, 289-310 (2019).

[46] Misawa, K. et al. Two extraterrestrial dust horizons found in the Dome Fuji ice core, East Antarctica. Earth Planet. Sci. Lett. 289, 287-297 (2010).

[47] Catling, D. C. et al. Atmospheric Origins of Perchlorate on Mars and in the Atacama. J. Gephys. Res. Planet 115, E00E11 (2010).

[48] Head, J. W., Marchant, D. R., Agnew, M. C., Fassett, C. I., Kreslawski, M. A. Extensive valley glacier deposits in the northern mid-latitudes of Mars: Evidence for Late Amazonian obliquity-driven climate change. Earth Planet. Sc. Lett. 241, 663-671 (2006).

[49] Kite, E. S., Matsuyama, I., Manga, M., Perron, J. T., Mitrovica, J. X. True Polar Wander driven by late-stage volcanism and the distribution of paleopolar deposits on Mars. Earth Planet. Sc. Lett. 280, 254-267 (2009).

[50] Tanaka, K. L. Dust and Ice Deposition in the Martian Geologic Record. Icarus 144, 254-266 (2000).

[51] Langevin, Y., Poulet, F., Bibring, J. P., Gondet, B. Sulfates in the North Polar Region of Mars Detected by OMEGA/Mars Express. Science 307, 1584-1586 (2005).

[52] Smith, I. B., Spiga, A., Holt, J. W. Aeolian processes as drivers of landform evolution at the South Pole of Mars. Geomorphology 240, 54-69 (2015).

[53] Hynek, B. M., McCollom, T. M., Szynkiewicz, A. Sulfur Cycling and Mass Balance at Meridiani, Mars. Geophys. Res. Lett. 46, 11728-11737 (2019).

[54] Albani, S. et al. Interpreting last glacial to Holocene dust changes at Talos Dome (East Antarctica): implications for atmospheric variations from regional to hemispheric scales. Clim. Past 8, 741-750 (2012).

[55] Hänel, G. The real part of the mean complex refractive index and the mean density of samples of atmospheric aerosol particles. *Tellus* **20**, 371-379 (1968).

[56] Delmonte, B., Petit, J. R., Maggi, V. Glacial to Holocene implications of the new 27000-year dust record from the EPICA Dome C (East Atarctica) ice core. *Clim. Dynam.* **18**, 647-660 (2002).

[57] Ruth, U. et al. Proxies and measurement techinques for mineral dust in Antarctic ice cores. *Environ. Sci. Technol.* **42**, 5675-5681 (2008).

[58] Ballabio, D. & Consonni, V. Classification tools in chemistry. Part 1: Linear models. PLS-DA. *Anal. Methods* **5**, 3790-3798 (2013).

[59] Dent, A. J. et al. B18: a core XAS spectroscopy beamline for Diamond. *J. Phys. Conf. Ser.* **190**, 012039 (2009).

[60] Macis, S. et al. Microdrop deposition technique: preparation and characterization of diluted suspended particulate samples. *Condensed Matt.* **3**, 21 (2018).

[61] Ravel, B. & Newville, M. ATHENA, ARTEMIS, HEPHAESTUS: data analysis for X-ray absorption spectroscopy using IFEFFIT. *J. Synchrotron Radiat.* **12**, 537-541 (2005).

[62] Calvin, S. XAFS for everyone. CRC Press - Taylor & Francis Group (2013).

[63] Cibin, G. et al. First combined total reflection X-ray fluorescence and grazing incidence X-ray absorption spectroscopy characterization of aeolian dust archived in Antarctica and Alpine deep ice cores. *Spectrochim. Acta B* **63**, 1503-1510 (2008).

[64] Shoenfelt, E. M., Winckler, G., Lamy, F., Anderson, R. F., Bostick, B. C. "Highly bioavailable dust-borne iron delivered to the Southern Ocean during glacial periods. *PNAS* **115**, 11180-11185 (2018).

[65] Formenti, P. et .al. Dominance of goethite over hematite in iron oxides of mineral dust from Western Africa: Quantitative partitioning by X-ray absorption spectroscopy. *J. Geophys. Res. Atmos.* **119**, 12740-12754 (2014).

[66] Zhang, X. L., Wu, J., Zhang, C. L., Xu, T. L., Zhou, Q. Q. What is the role of iron oxides in the optical properties of dust aerosols? *Atmos. Chem. Phys.* **15**, 12159-12177 (2015).

[67] Cong, Z. et al. Iron oxides in the cryoconite of glaciers on the Tibetan Plateau: abundance, speciation and implications. *Cryosphere* **12**, 3177-3186 (2018).

Supplementary Material to "Jarosite in Antarctic ice provides a window into acidic, water-limited weathering on Mars"

Giovanni Baccolo[1,2*], Barbara Delmonte[1], P. B. Niles[3], Giannantonio Cibin[4], Elena Di Stefano[1,2,5], Dariush Hampai[6], Lindsay Keller[3], Valter Maggi[1,2], Augusto Marcelli[6,7], Joseph Michalski[8], Christopher Snead[9] and Massimo Frezzotti[10].

[1]Department of Environmental and Earth Sciences, University of Milano-Bicocca, 20126, Milan, Italy
[2]INFN, section of Milano-Bicocca, 20126, Milan, Italy
[3]NASA Johnson Space Center, TX 77058, Houston, USA
[4]Diamond Light Source, Harwell Science and Innovation Campus, Didcot OX11 0DE, UK
[5]Department of Physical, Earth and Environmental Sciences, University of Siena, 53100, Siena, Italy
[6]Laboratori Nazionali di Frascati, Istituto Nazionale di Fisica Nucleare, 00044 Frascati, Italy
[7]Rome International Center for Materials Science - Superstripes, 00185 Rome, Italy
[8]Department of Earth Sciences, University of Hong Kong, Hong Kong
[9]Jacobs, NASA Johnson Space Center, TX 77058, Houston, USA
[10]Department of Science, University Roma Tre, Rome, Italy

* corresponding author: giovanni.baccolo@unimib.it

1. Jarosite Quantification

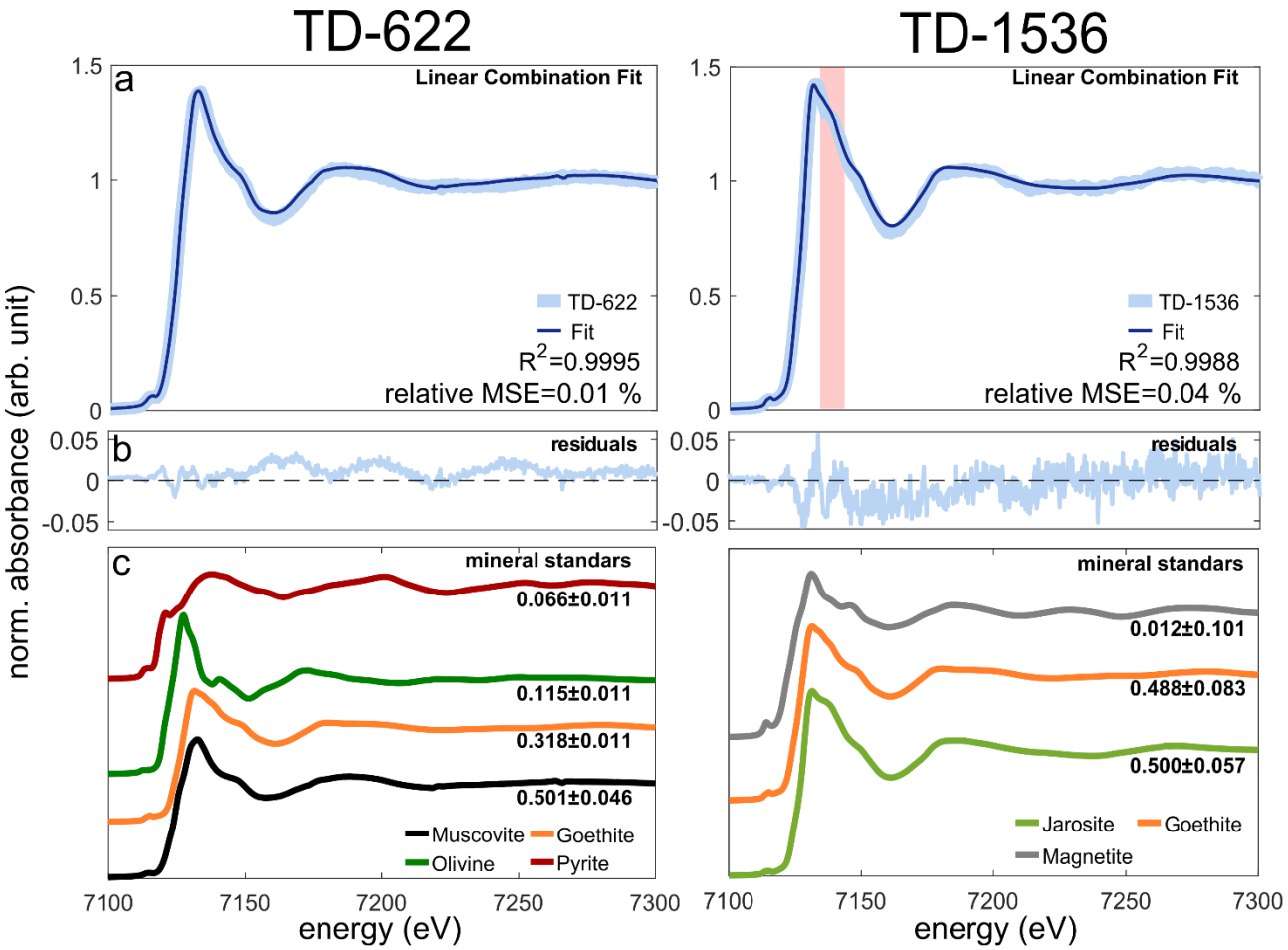

Figure S1 Examples showing the method for the estimation of jarosite within TALDICE mineral dust samples through Fe K-edge absorption spectroscopy. The sample on the left (from a depth of 622 m) is from the upper part of the core, the sample on the right from the deep part (from a depth of 1536 m), where physical and chemical anomalies are found. The experimental spectrum of the two samples is shown in association to the one obtained through linear combination fitting (panel a and d), R-squared (R^2) and relative Mean Square Error (MSE) are also shown to evaluate the goodness of fit. The red square highlight the position of the spectral convexity typical of jarosite [1]. Residuals are shown in panels b and e. Panels c and f refer to the spectra of the mineral standards that are present within the linear combinations used to reproduce the spectra of the samples, the number reported with uncertainties correspond to the coefficients defining such linear combinations. Uncertainties are statistical only and correspond to the errors derived from the application of the Ordinary Least Square algorithm.

The following approach was adopted to quantify the jarosite contribute within the Fe fraction of mineral dust extracted from TALDICE ice through Fe K-edge X-ray absorption spectroscopy:

1. Dust samples and mineral standards were analyzed at B18 Diamond beamline. For each of them Fe K-edge X-ray spectra were acquired.
2. Spectra were processed following the same procedure with the Athena software so as to make them fully comparable [2]. For each sample, multiple spectra were acquired and averaged in order to increase the signal to noise ratio. Spectra were calibrated and then normalized with respect to pre- and post-edge baselines.
3. Linear combination fitting was applied to highlight the minerals whose Fe fraction displayed a spectral signature compatible with the sample ones, following the procedures adopted by Shoenfelt et al. [3] and Liu et al. [4]. For each sample all the possible linear combinations of 4 standards (15 mineral standards were considered) were calculated, including the combinations defined by 3,2 and 1 standards. To limit computing time an assumption was made, that is the presence of goethite among the 4 standards. This decision has been taken because goethite is an extremely common Fe oxide in mineral dust aerosol, in particular in cold environments [5, 6, 7]. Considering this point, 377 linear models were calculated for each sample.
4. The best linear combination was selected considering the associated R^2 value. It always exceeded 0.9, confirming that the minerals selected as standards were well representative of TALDICE dust.
5. The 4 coefficients defining the best combination for each sample were inspected and in particular the one for jarosite, which was interpreted as a proxy for jarosite relative abundance. The high R^2 values confirmed that the selected combinations were well representative of the samples, in other words the information present in sample spectra was well reproduced by the calculated linear combinations. Since the sum of the 4 coefficients defining each combination is 1, the single coefficients of each mineral standard can be interpreted as the relative amount of information explained by the considered standard. Hypothesizing that a sample is well reproduced (R^2 near 1) by a single mineral standard with a coefficient near 1 means that all the information present within the sample spectrum is easily reproduced using that single mineral. In contrast, all the mineral standards not selected to define the best combination, were avoided by the algorithm because they didn't bring an improvement to the model.
6. Considering the previous point, the index presented in Figure 1c as "Jarosite % relative abundance" corresponds to the linear coefficient associated to jarosite within the best linear combination calculated for each sample. When the index is 0 (grey points in Figure 1c), it means that jarosite was not identified as one of the four best mineral standards to include within the model. When jarosite was considered, its linear coefficients were multiplied by 100 and reported in the graph as "Jarosite % relative abundance". The index is thus interpreted as the relative (%) amount of information contained within the sample spectra that is explained

by the presence of jarosite. It has to be intended as a relative index only and not as an absolute abundance index. The reason is that this index only refers to the jarosite contribute with respect to the Fe crystalline fraction of the minerals present within the samples, not to total dust concentration.

2. Additional SEM-EDX observations

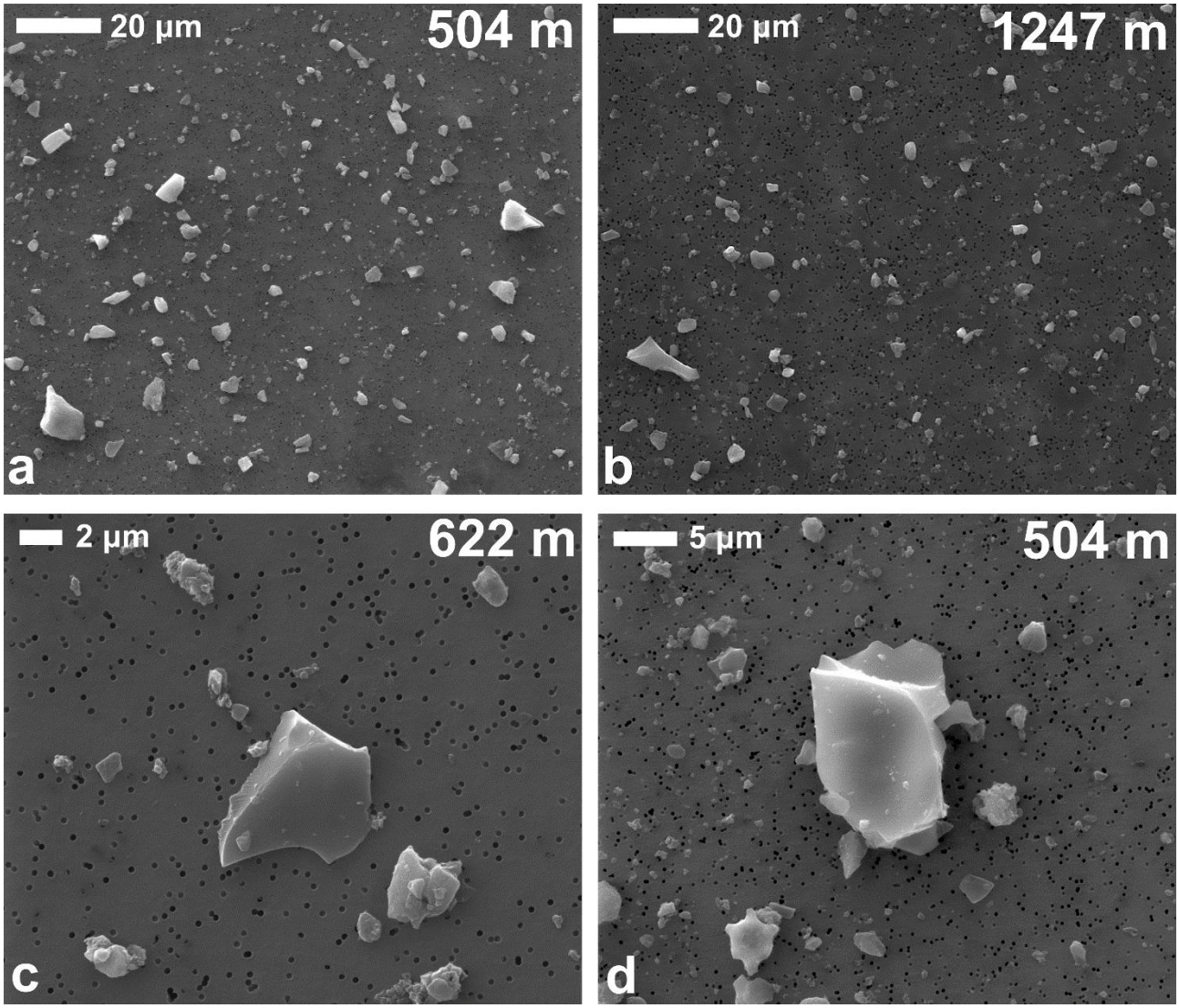

400

Figure S2 SEM images of dust particles extracted from ice sections in the upper part of TALDICE, courtesy of Biancamaria Narcisi. The morphological features of these particles are different from the ones which characterize the particles from the deepest part of TALDICE, for a comparison see Figure 2 in the main text. These images were acquired in the context of a previous work on TALDICE atmospheric mineral dust [8].

The mineral particles that are present in the upper part of TALDICE, where the mineral dust record is not affected by significant post-depositional processes, show a morphology well distinct from the one characterizing the particles from the deepest part of the core. As appreciated in Figure S2, mineral particles from the upper TALDICE sections mostly consist in volcanic shards and mono-mineral fragments with sharp edges and fresh textures. They are not aggregates of particles and lack weathering features as rounded edges, holes and depressions, which are common features in mineral particles entrapped in deep TALDICE (Figure 2 and Figure S3). Details about the construction of elemental maps through SEM-EDX is shown in Figure S4.

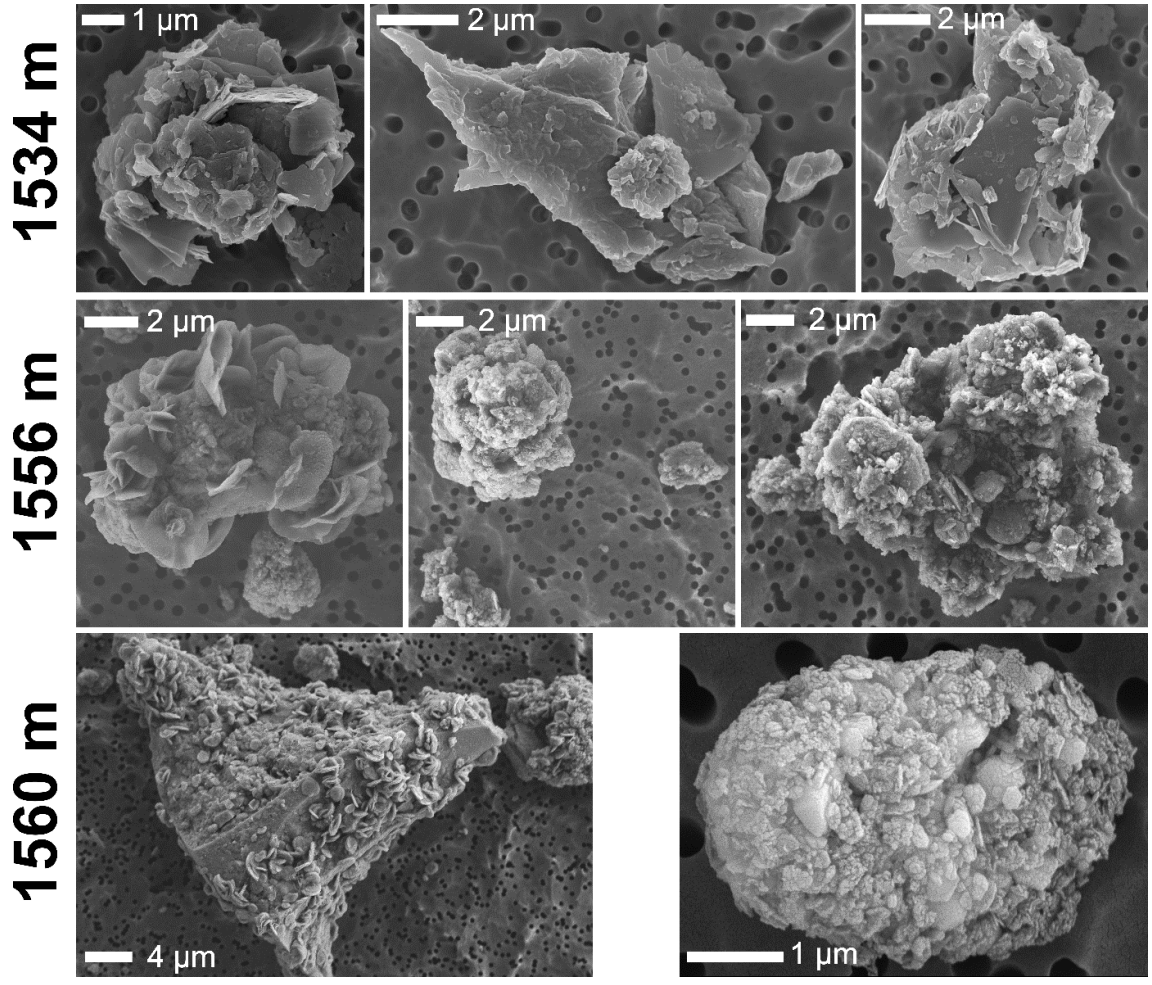

Figure S3 Additional SEM images of dust particles extracted from deep TALDICE samples.

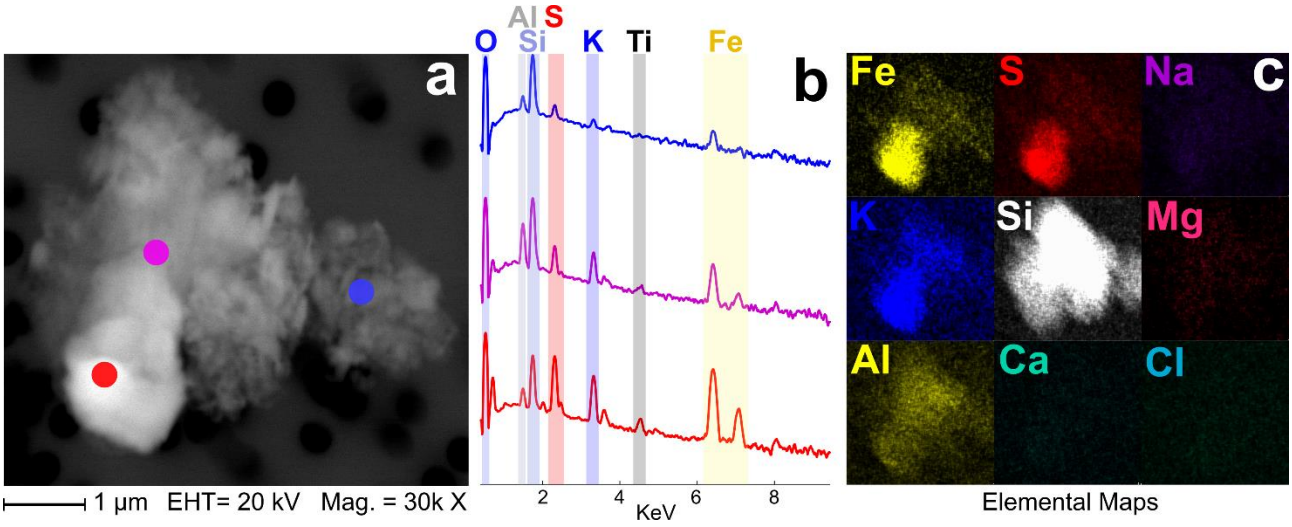

Figure S4 A detail of SEM-EDX analysis. Panel a: SEM picture of a dust particle from deep TALDICE ice. Panel b: 3 EDX spectra related to the areas of the particle highlighted by dots in panel s (paired colors). Major peaks are associated to the elements responsible for their emission with colored bands. Panel c: elemental maps of the particle. It can be seen that the brighter grain on the left (red dot) is mostly composed by S, Fe and K, compatible with jarosite; the core of the particle is richer in Si and Al, a composition pointing to amorphous silica with substituted Al.

3. TEM-EDX quantitative results

The two mineral grains investigated through TEM have also been analyzed with quantitative EDX spectroscopy to unveil their elemental composition. Results are shown in Tab. S1: it is noted that their composition is perfectly compatible with the jarosite one.

Element	Grain 1	Grain 2	Stoichmetric
Wt.%	Wt.%	Wt.%	jarosite
H	n.a.	n.a.	1.21
O	41.3	41.2	44.72
Al	0.5	0.7	-
Si	0.7	1.1	-
P	1.4	1.4	-
S	14.4	14.1	12.81
K	7.0	6.7	7.81
Ca	0.0	0.1	-
Ti	1.3	0.6	-
Fe	33.5	34.2	33.45
Total	100.0	100.0	100.00

n.a. – not analyzed

4. Correlation study

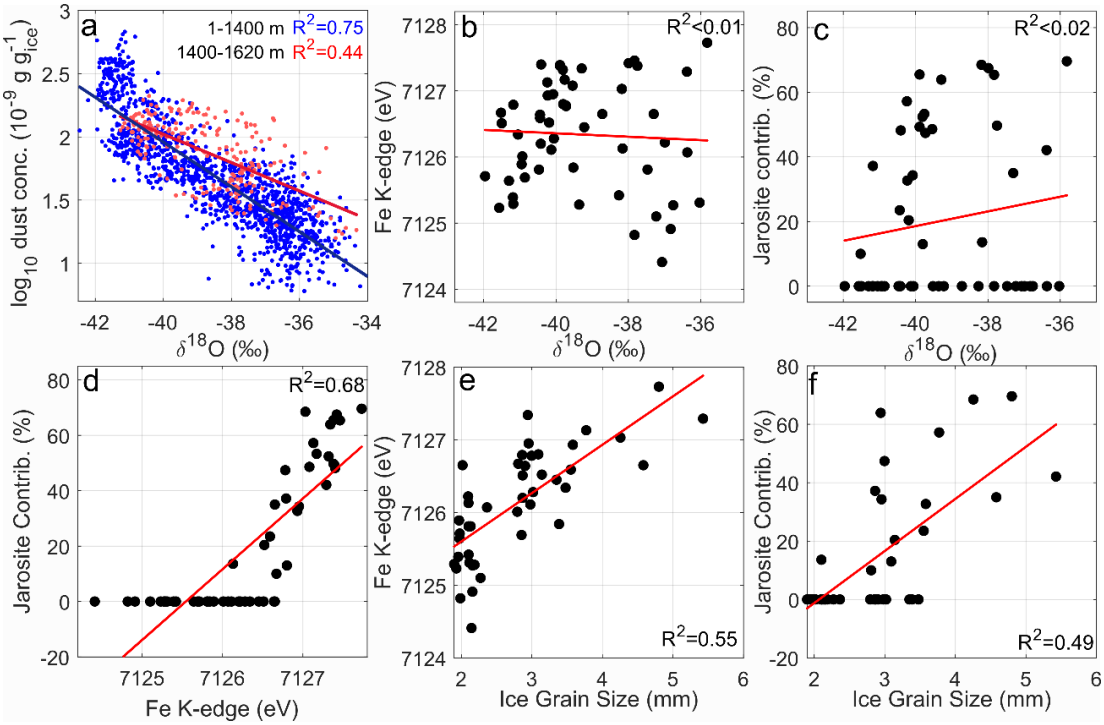

Figure S5 Linear correlation between the TALDICE records considered in this study. a) water $\delta^{18}O$ (data from Stenni et al. [9]) vs. $\log_{10}$ of dust concentration within ice considering the shallow part of TALDICE (blue dots) and the deepest one (below 1400 m, red dots); part of the data from [10, 11]. b) water $\delta^{18}O$ vs. Fe K-edge absorption energy of mineral dust. c) water $\delta^{18}O$ vs. jarosite contribution in dust samples. d) Fe K-edge absorption energy vs. jarosite contribution in dust samples. e) Fe-K edge absorption energy vs. the size of ice grain size along the TALDICE core (data from Montagnat et al. [12]). f) Jarosite contribution in TALDICE dust samples vs. the size of ice grain size along the TALDICE core.

5. Grain-size distributions

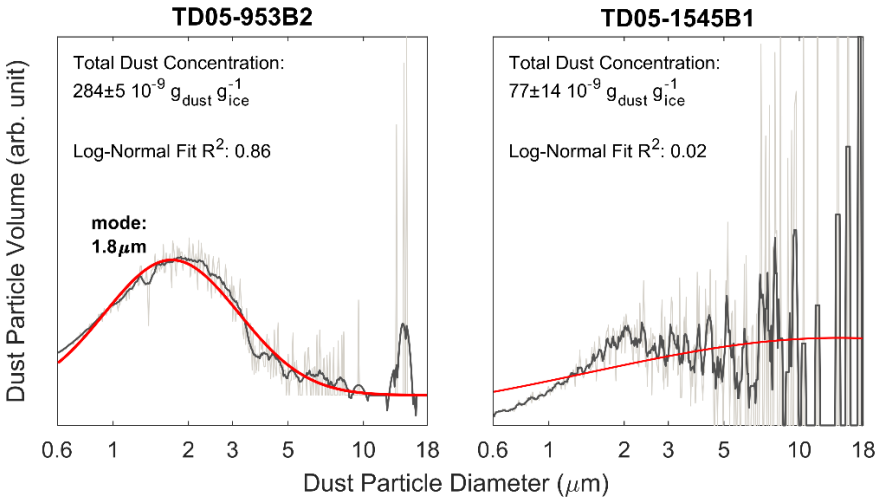

Figure S6 Examples of granulometric distributions from TALDICE dust samples from Coulter counter analysis. On the left a sample from the shallow part of the core (953 m deep), where geochemical anomalies are not observed. The grain size is well reproduced using a log-normal distribution, a common feature of mineral dust extracted from East Antarctica ice [13] and indicative of prolonged atmospheric transport before deposition. On the right a sample from the deep part of the core (1545 m deep), where Fe oxidation and jarosite are found. The log-normal distribution is not suited for these samples, where an excess of dust coarser than 5 μm and a lack of the one smaller than 2 μm are observed with respect to typical Antarctic grain size distributions.

6. Development of the "dust grain size" index

To develop the "grain size" index which highlighted the granulometric differences between dust samples from the upper and lower part of TALDICE, a Partial Least Square algorithm (PLS-DA) was applied [14]. The starting point for the application of the algorithm was the preparation of 16 variables defined to describe the 1517 samples measured through Coulter counter, they are:

1. Concentration within the 0.6-1.0 μm size interval
2. Concentration within the 1.0-2.0 μm size interval
3. Concentration within the 2.0-3.0 μm size interval
4. Concentration within the 3.0-4.0 μm size interval
5. Concentration within the 4.0-5.0 μm size interval
6. Concentration within the 0.6-5.0 μm size interval
7. Concentration within the 5.0-10.0 μm size interval
8. Concentration within the 0.6-10.0 μm size interval
9. Coarse local particle percentage (CLPP): $\frac{dust\ conc._{5-10\ \mu m}}{dust\ conc._{0.6-10\ \mu m}}$
10. Fine particle percentage (FPP): $\frac{dust\ conc._{0.6-2\ \mu m}}{dust\ conc._{0.6-5\ \mu m}}$
11. Coarse particle percentage (CPP): $\frac{dust\ conc._{3-5\ \mu m}}{dust\ conc._{0.6-5\ \mu m}}$
12. Concentration within the 10.0-18.0 μm size interval
13. $\frac{dust\ conc._{0.6-3\ \mu m}}{dust\ conc._{5-10\ \mu m}}$
14. $\frac{dust\ conc._{0.6-2\ \mu m}}{dust\ conc._{5-10\ \mu m}}$
15. $\frac{dust\ conc._{0.6-1\ \mu m}}{dust\ conc._{5-10\ \mu m}}$

16. $\frac{dust\ conc._{0.6-3\ \mu m}}{dust\ conc._{10-18\ \mu m}}$

After having defined these variables, samples were divided into shallow and deep in accordance to their depth: class "shallow" was applied to samples above 1450 m, "deep" to samples below 1450 m, where the geochemical and physical anomalies are evident. A first evaluation about the role of each one of the 16 variables with respect to the classification of the samples was carried out through multiple linear regression. Seventeen linear models were calculated: 1 considering all the variables and 16 excluding one variable at a time. For each of the models the associated R-squared was determined, results are shown in Figure S7 as absolute R-squared values (panel a) and relative (%) contribution of

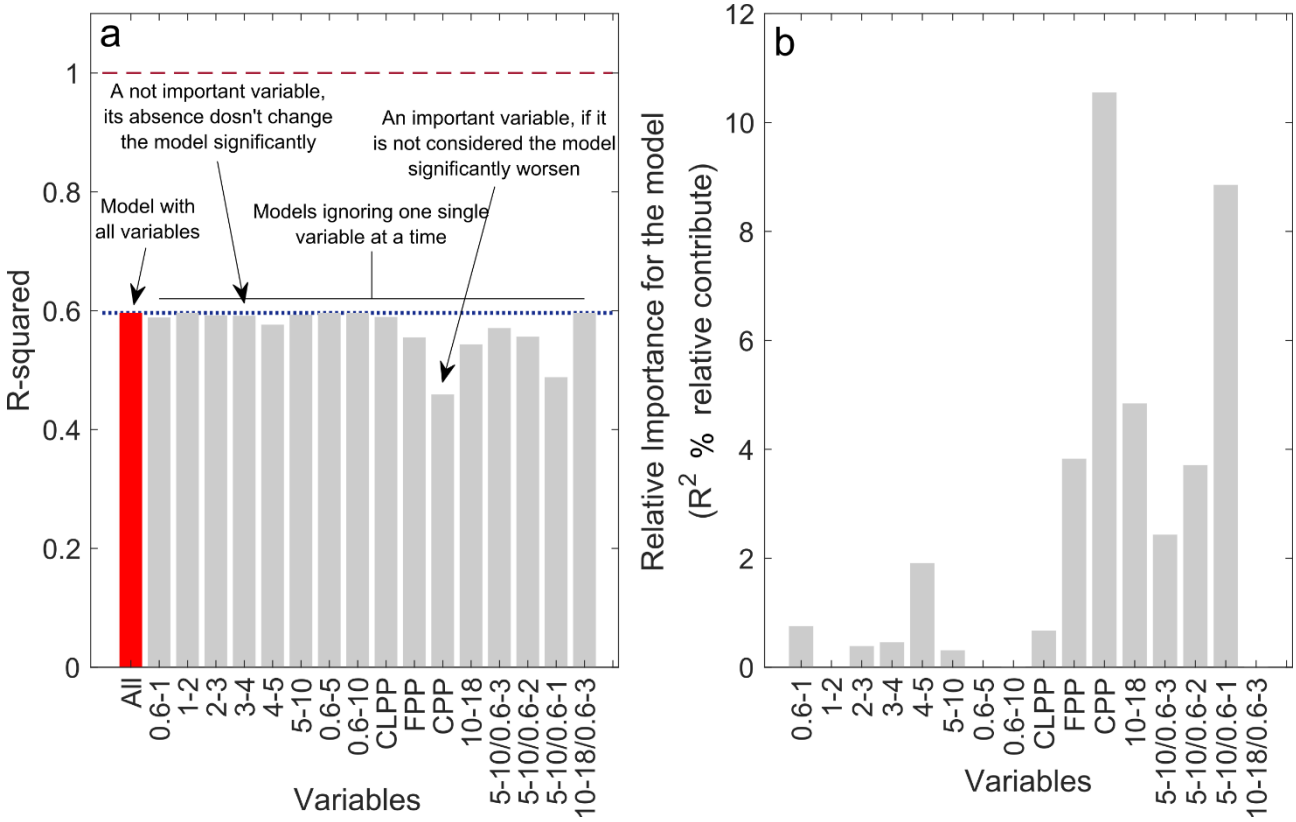

Figure S7 Multiple linear models calculated to classify shallow and deep TALDICE dust samples on the basis of their granulometric features. Panel a: R-squared associated to the 17 calculated models. Panel b: the relative contribution of the single variables with respect to the performances of the complete model. It is expressed in terms of relative difference of R-squared related to the complete model and the one associated to the models calculated excluding the single variables.

each variable in determining the R-squared coefficient of the complete model. The complete model has an R-squared coefficient of 0.59 and the most important variables are CPP and the ratio between the dust concentration of the 5-10 and

0.6-1 µm size intervals. Other variables, such as FPP, the concentration of the particles between 10 and 18 µm, the 5-10/0.6-3, 5-10/0.6-2 µm interval ratios have a secondary role, while the other are negligible (Figure S7b).

After this evaluation, the PLS-DA algorithm [14] was applied to reproduce the distinction between "shallow" and "deep" samples, still considering the 16 defined variables as descriptors. The R-squared of the obtained model was 0.63, meaning that the model could correctly reproduce 63% of the variance present within sample data. Another way to appreciate the performance of the model is the confusion matrix, where the actual classification is compared to the predicted one (Table S2). In the table it is appreciated that 1400 of the 1401 "shallow" samples (99.9 %) and 78 of the 116 "deep" samples (65.5 %) were correctly classified.

		Predicted Classes		
		Upper	**Lower**	**Total**
True Classes	**Upper**	1400	1	1401
	Lower	38	78	116
	Total	1438	79	

Table S2 Classification performances of the PLS-DA algorithm represented through the confusion matrix, where actual and predicted classes are compared.

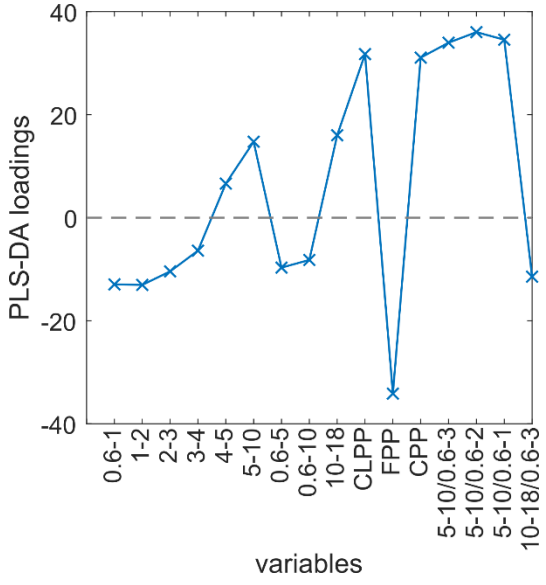

Figure S7 The loadings of the PLS-DA component which correspond to the "dust grain size" index presented in Figure 1d.

The "dust grain size" presented in Figure 1d corresponds to the PLS component which showed the maximum relative ability to correctly classify the samples among the 16 calculated ones. In Figure S7 the loadings of such component are shown in order to understand how the original variables contributed to the definition of the "dust grain size" index. It can be seen that the most important ones are the ratios between fine and coarse particle fractions and FPP (positive correlation with the index) and the CPP index (negative correlation).

7. References

[1] Johnstone, S. G. et al. Arsenic mobilization and iron transformations during sulfidization of As (V)-bearing jarosite. *Chem. Geol.* **334**, 9-24 (2012).

[2] Ravel, B. & Newville, M. ATHENA, ARTEMIS, HEPHAESTUS: data analysis for X-ray absorption spectroscopy using IFEFFIT. *J. Synchrotron Radiat.* **12**, 537-541 (2005).

[3] Shoenfelt, E. M., Winckler, G., Lamy, F., Anderson, R. F., Bostick, B. C. Highly bioavailable dust-borne iron delivered to the Southern Ocean during glacial periods. *PNAS* **115**, 11180-11185 (2018).

[4] Liu, S. et al. Iron Speciation in Insoluble Dust from High-Latitude Snow: An X-ray Absorption Spectroscopy Study. *Cond. Matter.* **3**, 47 (2018).

[5] Formenti, P. et al. Dominance of goethite over hematite in iron oxides of mineral dust from Western Africa: Quantitative partitioning by X-ray absorption spectroscopy. *J. Geophys. Res. Atmos.* **119**, 12740-12754 (2014).

[6] Zhang, X. L., Wu, G. J., Zhang, C. L., Xu, T. L., Zhou, Q. Q. What is the real role of iron oxides in the optical properties of dust aerosols?. Atm*os. Chem. Phys.* **15**, 12159-12177 (2015).

[7] Cong, Z. et al. Iron oxides in the cryoconite of glaciers on the Tibetan Plateau: abundance, speciation and implications. *Cryosphere* **12**, 3177-3186 (2018).

[8] Delmonte, B. et al. Modern and Holocene aeolian dust variability from Talos Dome (Northern Victoria Land) to the interior of the Antarctic ice sheet. *Quaternary Sci. Rev.* **64**, 76-89 (2013).

[9] Stenni, B. et al. Expression of the bipolar see-saw in Antarctic climate record during the last deglaciation. *Nat. Geosci.* **4**, 46-49 (2011).

[10] Albani, S. et al. Interpreting last glacial to Holocene dust changes at Talos Dome (East Antarctica): implications for atmospheric variations from regional to hemispheric scales. *Clim Past* **8**, 741-750 (2012).

[11] Baccolo, G. et al. The Contribution of Synchrotron Light for the Characterization of Atmospheric Mineral Dust in Deep Ice Cores: Preliminary Results from the Talos Dome Ice Core (East Antarctica). *Condensed Matt.* **3**, 25 (2018).

[12] Montagnat, M. et al. Measurements and numerical simulation of fabric evolution along the Talos Dome ice core, Antarctica. *Earth Planet. Sci. Lett.* **357-358**,168-178 (2012).

[13] Delmonte, B., Petit, J. R., Maggi, V. Glacial to Holocene implications of the new 27000-year dust record from the EPICA Dome C (East Atarctica) ice core. *Clim, Dynam,* **18**, 647-660 (2002).

[14] Ballabio, D. & Consonni, V. Classification tools in chemistry. Part 1: Linear models. PLS-DA. *Anal. Methods* **5**, 3790-3798 (2013).